Nano Research 2018, 11(3): 1415–1425
https://doi.org/10.1007/s12274-017-1757-2
Research Article

ISSN 1998-0124
CN 11-5974/O4

Hierarchical Ni-Co-S@Ni-W-O core–shell nanosheet arrays on nickel foam for high-performance asymmetric supercapacitors

Weidong He[1,§], Zhifu Liang[1,§], Keyu Ji[1], Qingfeng Sun[3] (✉), Tianyou Zhai[2] (✉), and Xijin Xu[1] (✉)

[1] *School of Physics and Technology, University of Jinan, 336 West Road of Nan Xinzhuang, Jinan 250022, China*
[2] *State Key Laboratory of Material Processing and Die & Mould Technology, School of Materials Science and Engineering, Huazhong University of Science and Technology (HUST), Wuhan 430074, China*
[3] *School of Engineering, Zhejiang A & F University, Hangzhou 311300, China*
§ *Weidong He and Zhifu Liang contributed equally to this work.*

Received: 22 May 2017
Revised: 1 July 2017
Accepted: 4 July 2017

KEYWORDS

core/shell structure,
free-standing electrode,
supercapacitors,
high energy density,
excellent stability

ABSTRACT

Nickel cobalt sulfides (Ni-Co-S) have attracted extensive attention for application in electronic devices owing to their excellent conductivity and high electrochemical capacitance. To facilitate the large-scale practical application of Ni-Co-S, the excellent rate capability and cyclic stability of these compounds must be fully exploited. Thus, hierarchical Ni-Co-S@Ni-W-O (Ni-Co-S-W) core/shell hybrid nanosheet arrays on nickel foam were designed and synthesized herein via a facile three-step hydrothermal method, followed by annealing in a tubular furnace under argon atmosphere. The hybrid structure was directly assembled as a free-standing electrode, which exhibited a high specific capacitance of 1,988 $F \cdot g^{-1}$ at 2 $A \cdot g^{-1}$ and retained an excellent capacitance of approximately 1,500 $F \cdot g^{-1}$ at 30 $A \cdot g^{-1}$, which is superior to the performance of the pristine Ni-Co-S nanosheet electrode. The assembled asymmetric supercapacitors achieved high specific capacitance (155 $F \cdot g^{-1}$ at 1 $A \cdot g^{-1}$), electrochemical stability, and a high energy density of 55.1 $W \cdot h \cdot kg^{-1}$ at a power density of 799.8 $W \cdot kg^{-1}$ with the optimized Ni-Co-S-W core/shell nanosheets as the positive electrode, activated carbon as the negative electrode, and 6 M KOH as the electrolyte.

1 Introduction

Supercapacitors (SCs) are a new type of energy storage device and are widely investigated for applications in portable electronics and electric vehicles [1–7]. In particular, pseudocapacitors, which store energy via fast, reversible, multi-electron, surface Faradaic redox reactions on electrode materials, can deliver a much higher specific capacitance than electrochemical double-layer capacitors (EDLCs), and thus hold great promise

---

Address correspondence to Tianyou Zhai, zhaity@hust.edu.cn; Qingfeng Sun, qfsun@zafu.edu.cn; Xijin Xu, sps_xuxj@ujn.edu.cn

for the construction of high-energy storage devices [8–12]. Nevertheless, the poor charge transfer ability of pseudocapacitive materials, such as transition metal oxides and hydroxides, hinders the large-scale practical application of supercapacitors to a great degree [13–18].

More recently, transition metal sulfides (TMS), especially bimetallic nickel cobalt sulfides, have attracted extensive attention owing to their excellent conductivity relative to that of the oxide/hydroxide counterparts and their higher specific capacitance compared with that of carbon-based materials [19–24]. Compared with monometallic sulfides (such as nickel sulfide or cobalt sulfide), the multiple valency contributions from both nickel and cobalt ions in the bimetallic sulfides can provide relatively rich redox reactions, resulting in higher specific capacitance and electric conductivity [25–28]. However, one of the major drawbacks of bimetallic sulfides is the low rate capability at fast charge/discharge rates [29, 30]. Therefore, the search for novel materials/architectures with outstanding electrochemical performance has become more and more essential.

Two strategies are commonly employed for the rational design of electrode materials with well-defined micro/nanostructures to obtain acceptable electrochemical performance. One approach involves fabricating composites and hybrid materials that can provide more accessible redox reaction sites, short ion and electron transport pathways, and a greater contact area between the electrode and electrolyte [31–35]. Another effective approach is the direct growth of electroactive materials on conductive substrates as binder-free electrodes, which can significantly increase the electric contact between the electroactive materials and the substrates, thus leading to short ion diffusion pathways [36–38]. More importantly, the 3D array nanostructure can greatly enhance the electron conductivity, thereby enabling better contact between the electroactive materials and the electrolyte to promote the Faradaic reactions for energy storage [39–41].

Nickel tungstate has been investigated as a promising material for electrochemical supercapacitors due to its higher electrical conductivity relative to nickel oxide and nickel molybdate because of the various valence states of W [42, 43]. However, the low energy density, poor rate capability, and disordered morphology limit its further application [44, 45]. Therefore, the design and synthesis of hierarchical Ni-Co-S@Ni-W-O core–shell hybrid materials may combine the advantages of both Ni-Co-S and Ni-W-O, leading to unprecedented electrochemical performance [46–48].

In this study, we present the rational design and synthesis of 3D hierarchical Ni-Co-S@Ni-W-O core–shell hybrid nanoarchitectures on a nickel foam scaffold, as free-standing electrodes, via a facile three-step hydrothermal method with subsequent annealing in a tubular furnace under argon atmosphere (Fig. 1).

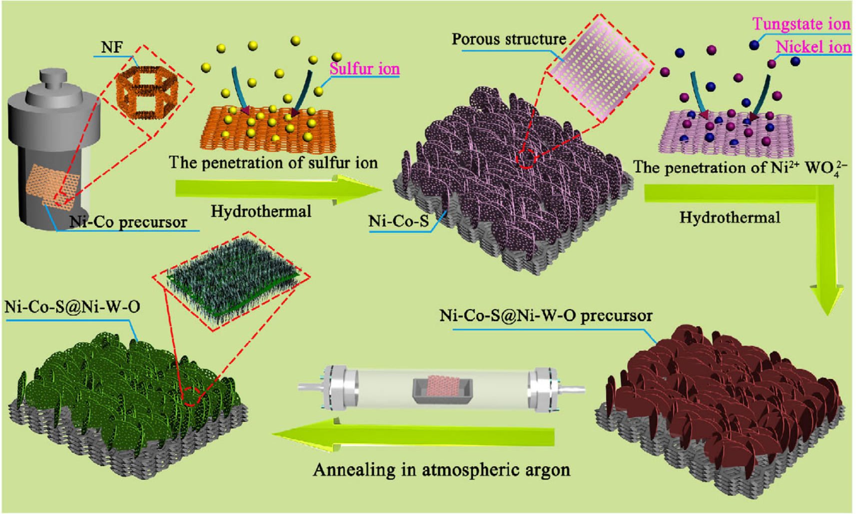

Figure 1 Schematic of preparation of networked Ni-Co precursor/Ni foam, Ni-Co-S/Ni foam electrode, and Ni-Co-S@Ni-W-O/Ni foam electrode (Ni-Co-S-W/NF).

The hybrid electrode exhibits a high specific capacitance of 1,988 $F\cdot g^{-1}$ at 2 $A\cdot g^{-1}$ and an excellent rate capability of 75.5% at 30 $A\cdot g^{-1}$. The as-assembled asymmetric supercapacitors achieve a high energy density of 55.1 $W\cdot h\cdot kg^{-1}$ at a power density of 799.8 $W\cdot kg^{-1}$, as well as excellent specific capacitance (155 $F\cdot g^{-1}$ at 1 $A\cdot g^{-1}$) and electrochemical stability.

2 Experimental

2.1 Synthesis of Ni-Co precursor on Ni foam

All chemicals used in this experiment were of analytical grade. Firstly, nickel foam (2 cm × 2 cm) was treated by ultrasonication in 3 M HCl solution for 10 min to remove the oxide on the surface and cleaned with ethanol and deionized water. In a typical synthesis, 0.29 g of $Co(NO_3)_2\cdot 6H_2O$, 0.145 g of $Ni(NO_3)_2\cdot 6H_2O$ and 0.6 g of hexamethylenetetramine (HMT) were dissolved in 30 mL of methanol under constant magnetic stirring to form a clear solution. The obtained solution was then transferred to a 50 mL Teflon-lined stainless steel autoclave with a piece of treated nickel foam (NF) immersed in the solution and maintained at 180 ℃ for 12 h. After cooling to room temperature, the Ni foam was removed and rinsed with deionized water and ethanol to remove any possible contamination on the surface, and finally dried at 60 ℃ for 12 h in a vacuum oven.

2.2 Synthesis of ultrathin Ni-Co-S nanosheet arrays on Ni foam

Typically, 0.3 g of C_2H_5NS was dissolved in 30 mL of deionized water and the solution was subsequently transferred to a Teflon-lined stainless steel autoclave along with the Ni-Co precursor/NF and kept at 140 ℃ for 5 h. After cooling the solution, the product was washed and dried as step one.

2.3 Synthesis of three-dimensional (3D) Ni-Co-S@Ni-W-O hybrid structures on Ni foam

To obtain the Ni-Co-S@Ni-W-O core–shell structures, 0.237 g of $NiCl_2\cdot 6H_2O$ and 0.3295 g of $Na_2WO_4\cdot 2H_2O$ were first dissolved in 30 mL of deionized (DI) water. The solution was transferred to a 50 mL Teflon-lined stainless steel autoclave, and the nickel foam with Ni-Co-S was added. The autoclave was kept at 130 ℃ for respective reaction time of 20, 40, and 80 min. Eventually, the Ni-Co-S@Ni-W-O hybrid structures on Ni foam were obtained by annealing under argon atmosphere at 350 ℃ for 2 h at a heating rate of 1 $℃\cdot min^{-1}$. The corresponding samples were denoted as Ni-Co-S-W (20 min)/NF, Ni-Co-S-W (40 min)/NF, and Ni-Co-S-W (80 min)/NF, respectively.

2.4 Material characterization

The morphologies and elemental composition of the as-prepared samples were characterized by field emission scanning electron microscopy (FESEM, FEI QUANTA FEG250) with energy dispersive X-ray spectrometry (EDS). The phases and structures were examined by X-ray diffraction (XRD, D8-Advance, Bruker) using Cu-Kα (λ = 0.15418 nm) irradiation. Transmission electron microscopy (TEM) data were acquired with an FEI TECNAI F20 microscope operating at an accelerating voltage of 200 kV. High-resolution X-ray photoelectron spectroscopy (XPS) measurements for evaluation of the elemental species and their chemical states were carried out on a Thermo ESCALAB250Xi instrument with a resolution of 0.43 eV.

2.5 Assembly of asymmetrical supercapacitors

The negative electrode was prepared by mixing activated carbon (TF-B520, ShangHai Carbosino Material Co., Ltd.), acetylene black (conductive additive), and polyvinylidene fluoride (PVDF) binder in N-methylpyrrolidone (NMP) solvent in a weight ratio of 75:15:10 to obtain a slurry. The slurry was then coated onto a lean nickel foam current collector (2 cm × 2 cm) and dried for 12 h at 120 ℃ under vacuum. Finally, the fabricated electrode was compressed at 10 MPa with a Manual Compressing Machine. An asymmetric supercapacitor (ASC) device was assembled by using an activated carbon electrode (AC/NF) as the negative electrode, the Ni-Co-S-W (40 min)/NF core–shell hybrid nanostructure (2 cm × 2 cm) as the positive electrode, and porous glassy fibrous paper as a separator. The electrodes and separator were soaked in 6 M KOH for about 12 h.

Finally, the assembled devices were carefully sealed using parafilm to ensure stable performance of the device.

2.6 Electrochemical measurement

The electrochemical properties of the Ni-Co-S/NF and Ni-Co-S@Ni-W-O/NF electrodes were evaluated by using an electrochemical workstation (Metrohm Autolab PGSTAT302N) with a three-electrode configuration, in 6 M aqueous KOH. The prepared samples were used as the working electrodes, Pt foil as the counter electrode (CE), and a Hg/HgO electrode as the reference electrode (RE). The electrochemical properties were investigated by cyclic voltammetry (CV) with variation of the scan rate from 5 to 50 mV·s^{-1} at a potential between 0 and 0.7 V, galvanostatic charge/discharge (GCD) with current densities ranging from 2 to 30 A·g^{-1} at a potential of 0 to 0.5 V, and electrochemical impedance spectrometry (EIS) in the frequency range of 100 kHz to 0.01 Hz.

3 Results and discussion

3.1 Structural characterization

The process for fabricating the advanced hybrid electrode by growing Ni-W-O on the Ni-Co-S scaffold is illustrated in Fig. 1. First, the as-prepared Ni-Co precursor nanoflakes on Ni foam were converted to ultrathin and porous Ni-Co-S nanoflakes by hydrothermal anion-exchange reaction processes. Numerous pores were formed on the Ni-Co-S nanoflakes, plausibly by the release of H_2S formed by the decomposition of thioacetamide (TAA; CH_3CSNH_2) during the sulfurization step [49]. Secondly, the Ni-Co-S/Ni foam was immersed in an aqueous solution containing Ni^{2+} and WO_4^{2-}, thereby facilitating formation of the Ni-W precursor on the surfaces of the Ni-Co-S nanoflakes. Finally, the Ni-Co-S@Ni-W-O core–shell hybrid nanoarchitectures on Ni foam were obtained by annealing under argon atmosphere at 350 °C.

SEM images of the Ni-Co-S (40 min) nanosheet arrays on Ni foam are presented in Figs. 2(a)–2(c), demonstrating that the surfaces of the Ni foam were evenly covered by the nanosheets (~ 100 nm thickness). Furthermore, densely packed, highly-ordered nanoflakes (Figs. 2(b) and 2(c)) were interconnected and intersected forming a 3D networked structure. The energy dispersive spectroscopy (EDS) profiles (inset in Fig. 2(b)) indicate the presence of Ni, Co, and S. The TEM image (inset in Fig. 2(c)) reveals the porous structure of the Ni-Co-S nanosheets. Figures 3(d)–3(f) show the typical SEM images of the Ni-Co-S-W core–shell nanosheet arrays on Ni foam with hydrothermal reaction for 40 min. Compared with the Ni-Co-S nanosheets, the core–shell nanosheets were thicker (~ 250 nm thickness) due to the formation of Ni-W-O on the surfaces of the Ni-Co-S nanosheets. The high-magnification SEM images (Figs. 2(e) and 2(f)) show the uniform formation of flocculent Ni-W-O nanostructures on the surfaces of the Ni-Co-S nanosheets. Figure 2(g) indicates that the Ni-Co-Si-W (40 min) nanosheets grown on the nickel foam are ca. 2 μm in width. The corresponding EDS data and mapping images indicate the presence of Ni, Co, W, O, and S. The influence of the reaction time on the thickness of the nanosheets was also investigated, as shown in Fig. S1 in the Electronic Supplementary Material (ESM), from which it was apparent that the nanosheets became thicker with increasing reaction time.

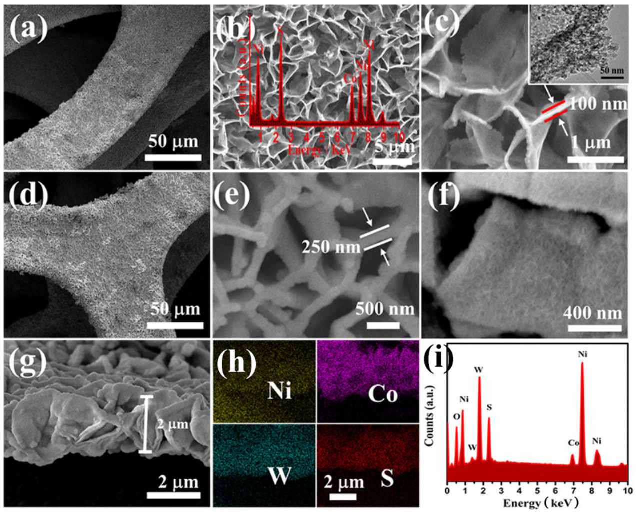

Figure 2 (a) Low and ((b) and (c)) high magnification SEM images of the Ni-Co-S/Ni foam; (d) low and ((e) and (f)) high magnification SEM images of Ni-Co-S-W (40 min) core–shell hybrid composite on Ni foam; (g)–(i) SEM, EDX, and corresponding elemental mapping images of Ni-Co-S-W (40 min) nanosheet arrays.

The crystal structures of the obtained Ni-Co-S nanosheets and Ni-Co-S-W hybrid nanosheets on Ni foam were studied by XRD, as shown in Fig. 3(a). The three strong peaks at 44.4°, 51.6°, and 76.1° are typical diffraction peaks from the Ni foam substrate. The major diffraction peaks at 26.8°, 31.6°, 38.3°, 50.5°, and 55.3° could be indexed to the (220), (311), (400), (511), and (440) crystal planes of cubic $NiCo_2S_4$ (JCPDS No. 20-0782). The XRD patterns of the Ni-Co-S-W hybrid nanosheets on foam show diffraction peaks at 24.0°, 24.9°, 36.6°, 54.6°, 62.3°, and 65.8°, which can be indexed to the (011), (110), (002), $(\bar{2}02)$, $(\bar{1}13)$, and $(\bar{3}11)$ crystal planes of monoclinic $NiWO_4$ (JCPDS No. 15-0755).

XPS measurements were used to explore the compositions and oxidation states of the elements in the Ni-Co-S-W (40 min) hybrid nanosheets, as shown in Figs. 3(b)–3(f). By using a Gaussian fitting method, the 4f spectrum (Fig. 3(b)) of W could be divided into three peaks at binding energies of 35.5, 33.6, and 37.7 eV, respectively, which correspond to W $4f_{7/2}$ (W^{6+} oxidation state) and elemental W [42, 44, 49]. The Ni 2p spectrum (Fig. 3(c)) was deconvoluted into two well-defined spin-orbit doublets, which are attributed to Ni^{2+} and Ni^{3+}, and two shakeup satellites [49]. The remarkable difference in the peak intensity of the two corresponding satellite peaks (noted as "Sat.") indicates that Ni^{2+} is dominant. In the XPS spectrum of Co 2p (Fig. 3(d)), the strong peaks at 778.9 eV for Co $2p_{3/2}$ and 794.1 eV for Co $2p_{1/2}$ are indicative of Co^{3+} [28, 29]. In the S 2p spectrum (Fig. 3(e)), the peak centered at 168.8 eV can be fitted to one main peak and one shakeup satellite peak. The main peak is assigned to the surface sulfur species in certain higher oxidation states. The peaks at binding energies of 161.6 and 162.6 eV correspond to the $S2p_{1/2}$ and $S2p_{3/2}$ states, respectively (Fig. 3(e)), demonstrating the presence of metal–sulfur bonds and S^{2-} [19, 50]. The peak at 529.8 eV in the O 1s XPS spectrum is typical of the metal–oxygen bonds, and the peak at 531.1 eV can be attributed to the physically adsorbed water on the surface [42]. Therefore, the product contains W^{6+}, Co^{2+}, Co^{3+}, Ni^{2+}, Ni^{3+}, and S^{2-}; this is in good agreement with the XRD data for Ni-Co-S-W/NF.

3.2 Electrochemical performance of Ni-Co-S-W/NF electrode

Figure 4(a) shows the CV curves of the Ni-Co-S-W (40 min) nanosheet arrays supported on nickel foam at various scan rates from 5 to 50 mV·s^{-1}. With an increase in the sweep rate, the integrated areas of the CV curves became larger, indicating higher

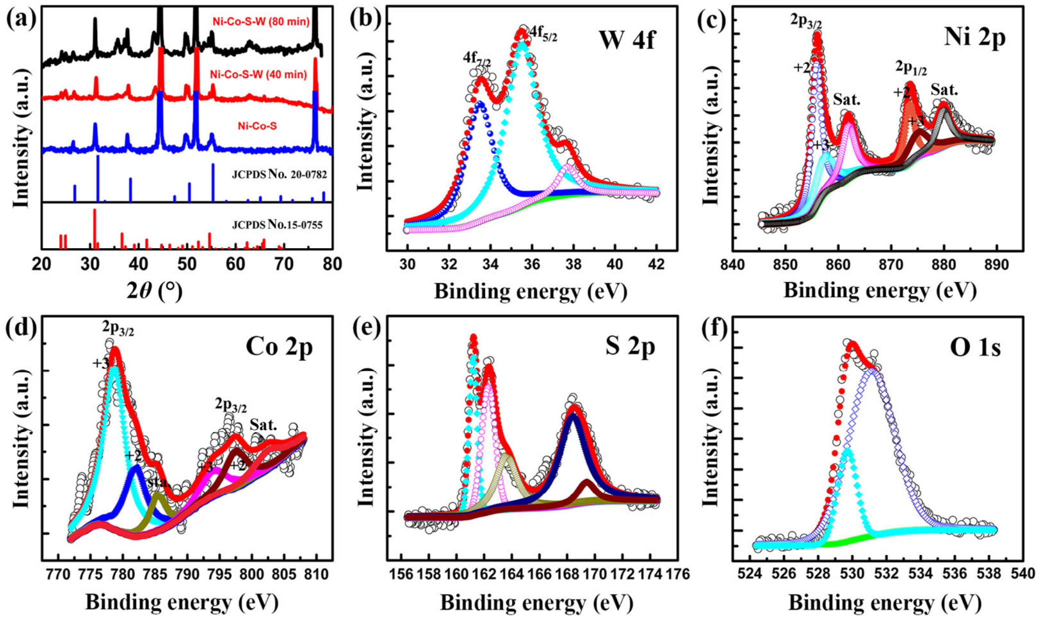

Figure 3 (a) XRD patterns of Ni-Co-S, Ni-Co-S-W (40 min), and Ni-Co-S-W (80 min) on nickel foam; (b) W 4f; (c) Ni 2p; (d) Co 2p; (e) S 2p, and (f) O 1s for Ni-Co-S-W (40 min) nanosheet arrays.

capacitance. Concomitantly, the anodic peaks shifted to the positive direction, and the cathodic peaks shifted to the negative direction, implying relatively low resistance and fast redox reactions at the interface of the electrode and electrolyte [19, 29]. The GCD curves in Fig. 4(b) exhibited a symmetrical shape over a wide current density from 2 to 30 A·g^{-1}, revealing high coulombic efficiency and good electrochemical capacitive characteristics due to the highly reversible redox reactions of the Ni-Co-S-W (40 min)/NF electrode in the charge–discharge process. For comparison, the CV curves of different hybrid electrodes at a constant scan rate of 20 mV·s^{-1} are shown in Fig. 4(c). The integrated area of the CV curve of the Ni-Co-S-W (40 min)/NF electrode is apparently larger than that of the other electrode materials, which can be attributed to the suitable reaction time as well as the core–shell nanosheet array structure. The Ni-Co-S-W (40 min)/NF electrode exhibited the longest discharge time, as shown in Fig. 4(d), which agrees well with the CV data presented in Fig. 4(c). The calculated specific capacitances for the pure Ni-Co-S/NF, Ni-Co-S-W (20 min)/NF, Ni-Co-S-W (80 min)/NF, and Ni-Co-S-W (40 min)/NF electrodes were respectively 1,270, 1,614, 1,280, and 1,970 F·g^{-1} at a current density of 3 A·g^{-1}. Figure 4(e) shows that the as-synthesized Ni-Co-S-W (40 min)/NF and Ni-Co-S-W (80 min)/NF electrodes exhibited better rate capability (84.6% and 98.2%, respectively) than the Ni-Co-S (38.4%) and Ni-Co-S-W (20 min) (75.5%) electrodes at 30 A·g^{-1}. EIS was used to confirm the good electrical conductivity of the Ni-Co-S-W (40 min)/NF electrode.

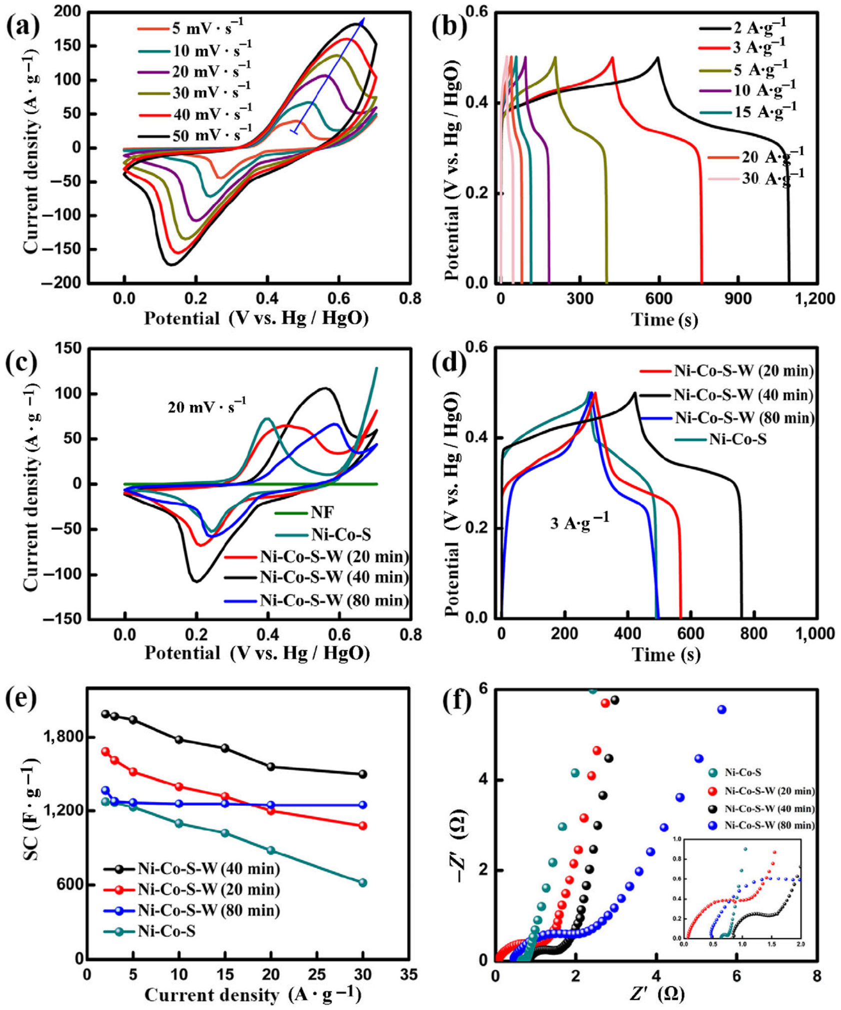

Figure 4 Electrochemical performance of the samples: (a) and (b) CV and GCD curves of Ni-Co-S-W (40 min)/NF; (c) and (d) CV and GCD curves of hybrid nanoarchitectures; (e) specific capacitances and (f) EIS curves of different samples.

From the plots, the more vertical line for the Ni-Co-S-W (40 min)/NF electrode in the low frequency region reveals the lower diffusion resistance (R_w), suggesting efficient diffusion of the electrolyte ions into the pores of the electrodes [39, 51]. The charge transfer resistance (R_{ct}) of the Ni-Co-S-W (40 min)/NF electrode was observed to be lower than that of the other composite electrodes and higher than that of the Ni-Co-S/NF electrode, which can be attributed to the synergistic effect of Ni-Co-S and Ni-W-O and the fast Faradaic reaction during the charge/discharge processes [52, 53]. The data prove that the Ni-Co-S nanosheet arrays have good electrical conductivity and are suitable as a conducting framework. The favorable electric conductivity contributes to the outstanding electrochemical properties of the Ni-Co-S-W (40 min)/NF hybrid electrode.

3.3 Electrochemical performance of the Ni-Co-S-W (40 min)/NF//activated carbon asymmetric supercapacitor

An asymmetric device was assembled by employing the as-prepared Ni-Co-S-W (40 min)/NF as the positive electrode and AC/NF as the negative electrode, respectively, separated by porous glassy fibrous paper (Fig. 5(a)). Comparison of the CV curves of the Ni-Co-S-W (40 min)/NF electrode and the AC/NF electrode at a scan rate of 30 mV·s^{-1} shows that the respective working potential ranges were 0–0.7 V and −1.0–0 V. The CV curve of the AC/NF negative electrode exhibits a similar rectangular shape (Fig. S2(a) in the ESM), demonstrating the ideal double-layer capacitor behavior based on fast diffusion/adsorption of the electrolyte ions. Figure S2(b) (in the ESM) shows the GCD curves of AC/NF under current densities ranging from 1 to 10 A·g^{-1}. The highly linear and symmetrical curves with their charge counterparts demonstrate the excellent electrochemical reversibility of the AC/NF electrode. The specific capacitance of the AC/NF electrode can reach up to 214 F·g^{-1} at 1 A·g^{-1} and was even maintained at 200 F·g^{-1} at 10 A·g^{-1} (Fig. S2(c) in the ESM). From the CV curves of the ASC device (Fig. 5(c)) recorded in different voltage windows, the stable operating voltage could be

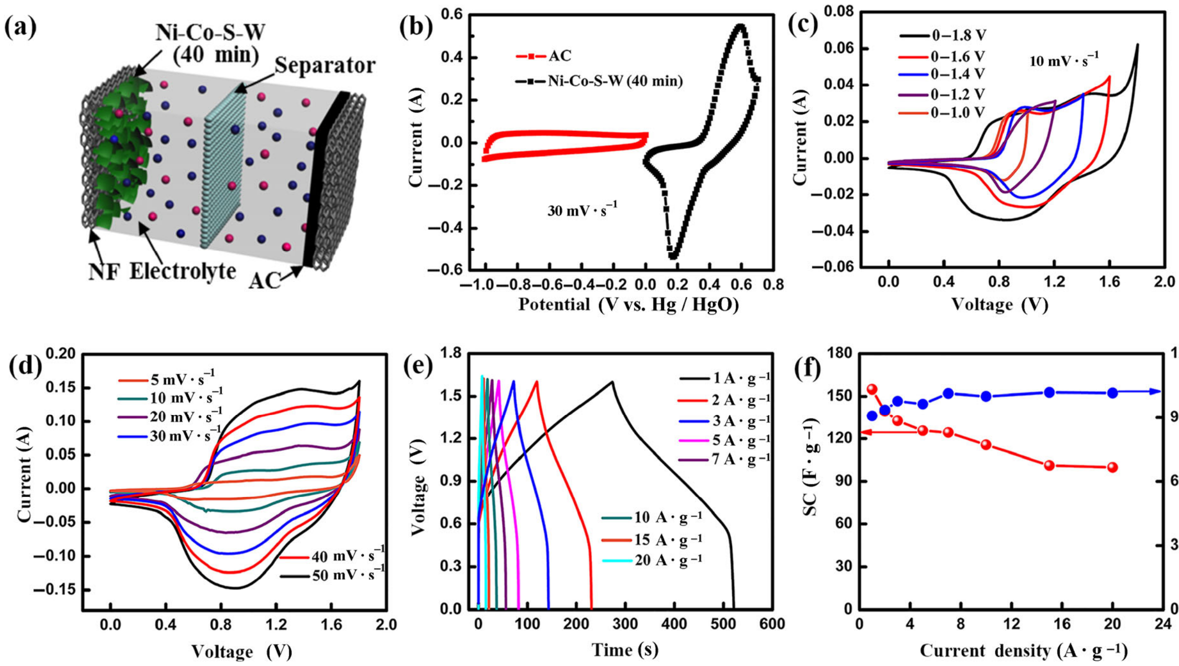

Figure 5 Electrochemical characterization of Ni-Co-S-W (40 min)/NF//AC/NF asymmetrical supercapacitors (ASCs): (a) schematic illustration of the ASCs; (b) comparison of CV curves collected for Ni-Co-S-W (40 min)/NF and AC/NF electrodes at a scan rate of 30 mV·s^{-1}; (c) CV curves collected over various potential windows at 10 mV·s^{-1}; (d) CV curves of ASCs at various scan rates ranging from 10 to 50 mV·s^{-1}; (e) GCD at various current densities in the voltage range of 0 to 1.6 V; (f) SCs and corresponding CE at different current densities.

extended to 1.8 V at a scan rate of 10 mV·s^{-1}. The CV curves obtained at various scan rates from 5 to 50 mV·s^{-1} demonstrate the collective contributions of the electric double-layer capacitance and pseudocapacitance at voltages ranging from 0 to 1.8 V (Fig. 5(d)). Furthermore, the almost symmetric GCD curves (Fig. 5(e)) indicate a high coulombic efficiency and electrochemical reversibility. The specific capacitance was calculated to be 155 F·g^{-1} at 1 A·g^{-1} (Fig. 5(f)), and remained at 100 F·g^{-1} with 65% of capacitance retention at 20 A·g^{-1}, providing further evidence of the high capacitance and excellent rate performance of the Ni-Co-S-W (40 min)/NF//AC/NF asymmetric supercapacitor.

The Ragone plots in Fig. 6(a) show that the ASCs in this study delivered an energy density as high as 55.1 W·h·kg^{-1} at the power density of 799.8 W·kg^{-1}; this energy density was still maintained at 35.5 W·h·kg^{-1} at the extremely high power density of 15,975 W·kg^{-1}. From comparison with other electrode materials (Fig. 6(a)), this performance is superior to those of $MnCo_2O_4$@$Ni(OH)_2$//AC [54], $NiCo_2O_4/MnO_2$//AC [55], Ni-Co-S/G//PCNS (G = graphene, PCNS = porous carbon nanosheets) [29], Ni-Co-S/$Co(OH)_2$//AC [9], $NiCo_2S_4$//AC [56], and $Ni_{0.67}Co_{0.33}MoO_4{\cdot}xH_2O$//AC [57]. The cycling performance of the asymmetric supercapacitors was evaluated at a current density of 1 A·g^{-1}; the ASCs displayed excellent cycling stability with retention of ~ 91.7% of the initial specific capacitance even after 6,000 cycles (Fig. 6(b)), indicating that the hybrid electrode has robust interconnected networks and good strain accommodation. To further demonstrate the practical use of the Ni-Co-S-W (40 min)/NF//AC/NF ASC device, two ASCs were connected in series (inset, Fig. 6(b)). A light emitting diode (LED) could be illuminated for more than 3 min, as shown in Fig. 6(c). These impressive results again confirm the excellent performance of the Ni-Co-S-W (40 min)/NF//AC/NF ASC device.

4 Conclusion

In summary, by using Ni-Co-S as a buffer and Ni-W-O as a shell, novel, hierarchical Ni-Co-S@Ni-W-O core–shell nanosheet arrays were constructed on nickel foam. The Ni-Co-S@Ni-W-O (40 min)/NF electrode exhibited low internal resistance as well as a high specific capacitance (1,988 F·g^{-1} at 2 A·g^{-1}) and retained an excellent capacitance ratio of 75.5% under extreme charge/discharge conditions (1,500 F·g^{-1} at 30 A·g^{-1}), which is superior to the performance of the pristine Ni-Co-S/NF electrode. The asymmetric supercapacitor achieved excellent specific capacitance (155 F·g^{-1} at 1 A·g^{-1}), electrochemical stability, and a high energy density of 55.1 W·h·kg^{-1} at a power density of 799.8 W·kg^{-1} with a cell voltage of 1.6 V. These excellent

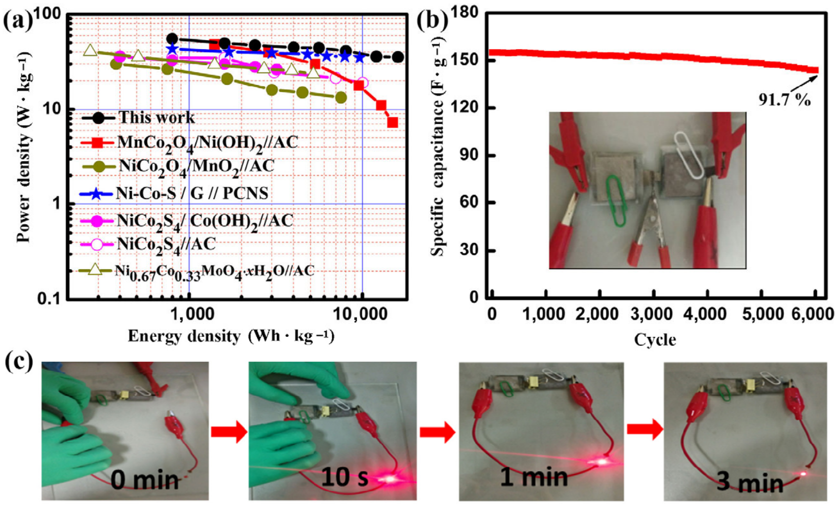

Figure 6 (a) Ragone plot illustrating energy and power densities of the Ni-Co-S-W (40 min)/NF//AC/NF asymmetrical supercapacitors; (b) cycling performance at a constant current density of 1 A·g^{-1}; (c) images of the blue LED at different stages.

electrochemical properties could be ascribed to the unique core–shell architecture and the synergistic effect of the Ni-Co-S nanosheets and the Ni-W-O.

Acknowledgements

This work was supported by the National Natural Science Foundation of China (No. 51672109), National Basic Research Program of China (No. 2015CB932600), Program for HUST Interdisciplinary Innovation Team (No. 2015ZDTD038) and the Fundamental Research Funds for the Central University (No. 2017KFKJXX007), Natural Science Foundation of Shandong Province for Excellent Young Scholars (No. ZR2016JL015), Scientific Research Foundation of Zhejiang A&F University (No. 2014FR077).

Electronic Supplementary Material: Supplementary material (low and high magnification SEM images of Ni-Co-S@Ni-W-O (20 min)/NF and Ni-Co-S@Ni-W-O (80 min)/NF, the CV and GCD curves of the activated carbon (AC)/NF, the specific capacitances of AC/NF at different current densities) is available in the online version of this article at https://doi.org/10.1007/s12274-017-1757-2.

References

[1] El-Kady, M. F.; Strong, V.; Dubin, S.; Kaner, R. B. Laser scribing of high-performance and flexible graphene-based electrochemical capacitors. *Science* **2012**, *335*, 1326–1330.

[2] Tang, S. C.; Zhu, B. G.; Shi, X. L.; Wu, J.; Meng, X. K. General controlled sulfidation toward achieving novel nanosheet-built porous square-$FeCo_2S_4$-tube arrays for high-performance asymmetric all-solid-state pseudocapacitors. *Adv. Energy Mater.* **2017**, *7*, 1601985.

[3] Dresselhaus, M. S.; Thomas, I. L. Alternative energy technologies. *Nature* **2001**, *414*, 332–337.

[4] Zhu, M. S.; Huang, Y.; Huang, Y.; Pei, Z. X.; Xue, Q.; Li, H. F.; Geng, H. Y.; Zhi, C. Y. Capacitance enhancement in a semiconductor nanostructure-based supercapacitor by solar light and a self-powered supercapacitor-photodetector system. *Adv. Funct. Mater.* **2016**, *26*, 4481–4490.

[5] Wen, L.; Li, F.; Cheng, H. M. Carbon nanotubes and graphene for flexible electrochemical energy storage: From materials to devices. *Adv. Mater.* **2016**, *28*, 4306–4337.

[6] Liu, L. L.; Niu Z. Q.; Chen J. Design and integration of flexible planar micro-supercapacitors. *Nano Res.* **2017**, *10*, 1524–1544.

[7] He, W. D.; Wang, C. G.; Li, H. Q.; Deng, X. L.; Xu, X. J.; Zhai, T. Y. Ultrathin and porous $Ni_3S_2/CoNi_2S_4$ 3D-network structure for superhigh energy density asymmetric supercapacitors. *Adv. Energy Mater.* **2017**, 1700983.

[8] Lu, F.; Zhou, M,; Li, W. R.; Weng, Q. H.; Li, C. L.; Xue, Y. M.; Jiang, X. F.; Zeng, X. H.; Bando, Y.; Golberg, D. Engineering sulfur vacancies and impurities in $NiCo_2S_4$ nanostructures toward optimal supercapacitive performance. *Nano Energy* **2016**, *26*, 313–323.

[9] Li, R.; Wang, S. L.; Huang, Z. C.; Lu, F. X.; He, T. B. $NiCo_2S_4@Co(OH)_2$ core-shell nanotube arrays *in situ* grown on Ni foam for high performances asymmetric supercapacitors. *J. Power Sources* **2016**, *312*, 156–164.

[10] Huang, Y.; Zhu, M. S.; Huang, Y.; Pei, Z. X.; Li, H. F.; Wang, Z. F.; Xue, Q.; Zhi, C. Y. Multifunctional energy storage and conversion devices. *Adv. Mater.* **2016**, *28*, 8344–8364.

[11] Huang, Y.; Tao, J. Y.; Meng, W. J.; Zhu, M. S.; Huang, Y.; Fu, Y. Q.; Gao, Y. H.; Zhi, C. Y. Super-high rate stretchable polypyrrole-based supercapacitors with excellent cycling stability. *Nano Energy* **2015**, *11*, 518–525.

[12] Liu, X. X.; Shi, C. D.; Zhai, C. W.; Cheng, M. L.; Liu, Q.; Wang, G. X. Cobalt-based layered metal-organic framework as an ultrahigh capacity supercapacitor electrode material. *ACS Appl. Mater. Interfaces* **2016**, *8*, 4585–4591.

[13] He, W. D.; Yang, W. J.; Wang, C. G.; Deng, X. L.; Liu, B. D.; Xu, X. J. Morphology-controlled syntheses of α-MnO_2 for electrochemical energy storage. *Phys. Chem. Chem. Phys.* **2016**, *18*, 15235–15243.

[14] Dong, L. B.; Xu, C. J.; Li, Y.; Wu, C. L.; Jiang, B. Z.; Yang, Q.; Zhou, E. L.; Kang, F. Y.; Yang, Q. H. Simultaneous production of high-performance flexible textile electrodes and fiber electrodes for wearable energy storage. *Adv. Mater.* **2016**, *28*, 1675–1681.

[15] Yang, J.; Yu, C.; Fan, X. M.; Zhao, C. T.; Qiu, J. S. Ultrafast self-assembly of graphene oxide-induced monolithic NiCo-carbonate hydroxide nanowire architectures with a superior volumetric capacitance for supercapacitors. *Adv. Funct. Mater.* **2015**, *25*, 2109–2116.

[16] Gu, S. S.; Lou, Z.; Li, L. D.; Chen, Z. J.; Ma, X. D.; Shen, G. Z. Fabrication of flexible reduced graphene oxide/Fe_2O_3 hollow nanospheres based on-chip micro-supercapacitors for integrated photodetecting applications. *Nano Res.* **2016**, *9*, 424–434.

[17] Guo, K.; Ma, Y.; Li, H. Q.; Zhai, T. Y. Flexible wire-shaped supercapacitors in parallel double helix configuration with stable electrochemical properties under static/dynamic bending. *Small* **2016**, *12*, 1024–1033.

[18] Wu, X.; Han, Z. C.; Zheng, X.; Yao, S. Y.; Yang, X.; Zhai, T. Y. Core-shell structured Co_3O_4@$NiCo_2O_4$ electrodes grown on flexible carbon fibers with superior electrochemical properties. *Nano Energy* **2017**, *31*, 410–417.

[19] Zhu, J.; Tang, S. C.; Wu, J.; Shi, X. L.; Zhu, B. G.; Meng, X. K. Wearable high-performance supercapacitors based on silver-sputtered textiles with $FeCo_2S_4$–$NiCo_2S_4$ composite nanotube-built multitripod architectures as advanced flexible electrodes. *Adv. Energy Mater.* **2017**, *7*, 1601234.

[20] Hou, L. R.; Shi, Y. Y.; Zhu, S. Q.; Rehan, M.; Pang, G.; Zhang, X. G.; Yuan, C. Z. Hollow mesoporous hetero-$NiCo_2S_4$/Co_9S_8 submicro-spindles: Unusual formation and excellent pseudocapacitance towards hybrid supercapacitors. *J. Mater. Chem. A* **2017**, *5*, 133–144.

[21] Dai, S. G.; Zhao, B. T.; Qu, C.; Chen, D. C.; Dang, D.; Song, B.; deGlee, B. M.; Fu, J. W.; Hu, C. G.; Wong, C. P. et al. Controlled synthesis of three-phase Ni_xS_y/rGO nanoflake electrodes for hybrid supercapacitors with high energy and power density. *Nano Energy* **2017**, *33*, 522–531.

[22] Niu, Z. Q.; Zhou, W. Y.; Chen, X. D.; Chen, J.; Xie, S. S. Highly compressible and all-solid-state supercapacitors based on nanostructured composite sponge. *Adv. Mater.* **2015**, *27*, 6002–6008.

[23] Li, Y. J.; Wang, G. L.; Wei, T.; Fan, Z. J.; Yan, P. Nitrogen and sulfur co-doped porous carbon nanosheets derived from willow catkin for supercapacitors. *Nano Energy* **2016**, *19*, 165–175.

[24] Xie, X. Q.; Makaryan, T.; Zhao, M. Q.; Van Aken, K. L.; Gogotsi, Y.; Wang, G. X. MoS_2 nanosheets vertically aligned on carbon paper: A freestanding electrode for highly reversible sodium-ion batteries. *Adv. Energy Mater.* **2016**, *6*, 1502161.

[25] Ji, H. M.; Liu, C.; Wang, T.; Chen, J.; Mao, Z. N.; Zhao, J.; Hou, W. H.; Yang, G. Porous hybrid composites of few-layer MoS_2 nanosheets embedded in a carbon matrix with an excellent supercapacitor electrode performance. *Small* **2015**, *11*, 6480–6490.

[26] Nguyen, V. H.; Shim, J. J. *In situ* growth of hierarchical mesoporous $NiCo_2S_4$@MnO_2 arrays on nickel foam for high-performance supercapacitors. *Electrochim. Acta* **2015**, *166*, 302–309.

[27] Hu, W.; Chen, R. Q.; Xie, W.; Zou, L. L.; Qin, N.; Bao, D. H. $CoNi_2S_4$ nanosheet arrays supported on nickel foams with ultrahigh capacitance for aqueous asymmetric supercapacitor applications. *ACS Appl. Mater. Interfaces* **2014**, *6*, 19318−19326.

[28] Khani H.; Wipf, D. O. Iron oxide nanosheets and pulse-electrodeposited Ni–Co–S nanoflake arrays for high-performance charge storage. *ACS Appl. Mater. Interfaces* **2017**, *9*, 6967–6978.

[29] Yang, J.; Yu, C.; Fan, X. M.; Liang, S. X.; Li, S. F.; Huang, H. W.; Ling, Z.; Hao, C.; Qiu, J. S. Electroactive edge site-enriched nickel-cobalt sulfide into graphene frameworks for highperformance asymmetric supercapacitors. *Energy Environ. Sci.* **2016**, *9*, 1299−1307.

[30] Li, X. M.; Li, Q. G.; Wu, Y.; Rui, M. C.; Zeng, H. B. Two-dimensional, porous nickel-cobalt sulfide for high-performance asymmetric supercapacitors. *ACS Appl. Mater. Interfaces* **2015**, *7*, 19316−19323.

[31] Guan, C.; Xia, X. H.; Meng, N.; Zeng, Z. Y.; Cao, X. H.; Soci, C.; Zhang, H.; Fan, H. J. Hollow core-shell nanostructure supercapacitor electrodes: Gap matters. *Energy Environ. Sci.* **2012**, *5*, 9085−9090.

[32] Li, Y.; Xu, J.; Feng, T.; Yao, Q. F.; Xie, J. P.; Xia, H. Fe_2O_3 nanoneedles on ultrafine nickel nanotube arrays as efficient anode for high-performance asymmetric supercapacitors. *Adv. Funct. Mater.* **2017**, *21*, 1606728.

[33] Lin, L. Y.; Tang, S.; Zhao, S. Q.; Peng, X. H.; Hu, N. Hierarchical three-dimensional $FeCo_2O_4$@MnO_2 core-shell nanosheet arrays on nickel foam for high-performance supercapacitor. *Electrochim. Acta* **2017**, *228*, 175–182.

[34] Zhou, S. S.; Chen, J. N.; Gan, L.; Zhang, Q.; Zheng, Z.; Li, H. Q.; Zhai, T. Y. Scalable production of self-supported WS_2/CNFs by electrospinning as the anode for high-performance lithium-ion batteries. *Sci. Bull.* **2016**, *61*, 227–235.

[35] Wang, X.; Zhang, S. W.; Shao, M. H.; Huang, J. Z.; Deng, X. L.; Hou, P. Y.; Xu, X. J. Fabrication of ZnO/$ZnFe_2O_4$ hollow nanocages through metal organic frameworks route with enhanced gas sensing properties. *Sensor Actuat. B Chem.* **2017**, *251*, 27–33.

[36] Zhou, W. J.; Cao, X. H.; Zeng, Z. Y.; Shi, W. H.; Zhu, Y. Y.; Yan, Q. Y.; Liu, H.; Wang, J. Y.; Zhang, H. One-step synthesis of Ni_3S_2 nanorod@$Ni(OH)_2$ nanosheet core-shell nanostructures on a three-dimensional graphene network for high-performance supercapacitors. *Energy Environ. Sci.* **2013**, *6*, 2216–2221.

[37] Dong, L. B.; Liang, G. M.; Xu, C. J.; Liu, W. B.; Pan, Z. Z.; Zhou, E. L.; Kang, F. Y.; Yang, Q. H. Multi hierarchical construction-induced superior capacitive performances of flexible electrodes for wearable energy storage. *Nano Energy* **2017**, *34*, 242–248.

[38] Liu, Z. H.; Tian, X. C.; Xu, X.; He, L.; Yan, M. Y.; Han, C. H.; Li, Y.; Yang, W.; Mai, L. Q. Capacitance and voltage matching between MnO_2 nanoflake cathode and Fe_2O_3 nanoparticle anode for high-performance asymmetric micro-supercapacitors. *Nano Res.* **2017**, *10*, 2471–2481.

[39] Zhang, Y. F.; Zuo, L. Z.; Zhang, L. S.; Yan, J. J.; Lu, H. Y.;

Fan, W.; Liu, T. X. Immobilization of NiS nanoparticles on N-doped carbon fiber aerogels as advanced electrode materials for supercapacitors. *Nano Res*. **2016**, *9*, 2747–2759.

[40] Lv, Q. Y.; Wang, S.; Sun, H. Y.; Luo, J.; Xiao, J.; Xiao, J. W.; Xiao, F.; Wang, S. Solid-state thin-film supercapacitors with ultrafast charge/discharge based on N-doped-carbon-tubes/Au-nanoparticles-doped-MnO_2 nanocomposites. *Nano Lett*. **2016**, *16*, 40−47.

[41] Wang, J.; Zhang, X.; Wei, Q. L.; Lv, H. M.; Tian, Y. L.; Tong, Z. Q.; Liu, X. S.; Hao, J.; Qu, H. Y.; Zhao, J. P. et al. 3D self-supported nanopine forest-like Co_3O_4@$CoMoO_4$ core-shell architectures for high-energy solid state supercapacitors. *Nano Energy* **2016**, *19*, 222–233.

[42] Chen, S. M.; Yang, G.; Jia Y.; Zheng, H. J. Three-dimensional $NiCo_2O_4$@$NiWO_4$ core-shell nanowire arrays for high performance supercapacitors. *J. Mater. Chem. A* **2017**, *5*, 1028–1034.

[43] He, G. J.; Li, J. M.; Li, W. Y.; Li, B.; Noor, N.; Xu, K. B.; Hu. J. Q.; Parkin, I. P. One pot synthesis of nickel foam supported self-assembly of $NiWO_4$ and $CoWO_4$ nanostructures that act as high performance electrochemical capacitor electrodes. *J. Mater. Chem. A* **2015**, *3*, 14272–14278.

[44] Xu, X. Y.; Gao, J. P.; Huang, G. B.; Qiu, H. X.; Wang, Z. Y.; Wu, J. Z.; Pan, Z.; Xing, F. B. Fabrication of $CoWO_4$@$NiWO_4$ nanocomposites with good supercapacitve performances. *Electrochim. Acta* **2015**, *174*, 837–845.

[45] Niu, L. Y.; Li, Z. P.; Xu, Y.; Sun, J. F.; Hong, W.; Liu, X. H.; Wang, J. Q.; Yang, S. R. Simple synthesis of amorphous $NiWO_4$ nanostructure and its application as a novel cathode material for asymmetric supercapacitors. *ACS Appl. Mater. Interfaces* **2013**, *5*, 8044−8052.

[46] He, W. D.; Wang, C. G.; Zhuge, F.; Deng, X. L.; Xu, X. J.; Zhai, T. Y. Flexible and high energy density asymmetrical supercapacitors based on core/shell conducting polymer nanowires/manganese dioxide nanoflakes. *Nano Energy* **2017**, *35*, 242–250.

[47] Kuang, M.; Liu, X. Y.; Dong, F.; Zhang, Y. X. Tunable design of layered $CuCo_2O_4$ nanosheets@MnO_2 nanoflakes core-shell arrays on Ni foam for high-performance supercapacitors. *J. Mater. Chem. A* **2015**, *3*, 21528–21536.

[48] Liao, J. Y.; Higgins, D.; Lui, G.; Chabot, V.; Xiao, X. C.; Chen, Z. W. Multifunctional TiO_2–C/MnO_2 core-double-shell nanowire arrays as high-performance 3D electrodes for lithium ion batteries. *Nano Lett*. **2013**, *13*, 5467–5473.

[49] Ma, L. B.; Hu, Y.; Chen, R. P.; Zhu, G. Y.; Chen, T.; Lv, H. L.; Wang, Y. R.; Liang, J.; Liu, H. X.; Yan, C. Z. et al. Self-assembled ultrathin $NiCo_2S_4$ nanoflakes grown on Ni foam as high-performance flexible electrodes for hydrogen evolution reaction in alkaline solution. *Nano Energy* **2016**, *24*, 139–147.

[50] Bai, D. X.; Wang, F.; Lv, J. M.; Zhang, F. Z.; Xu, S. L. Triple-confined well-dispersed biactive $NiCo_2S_4$/$Ni_{0.96}S$ on graphene aerogel for high-efficiency lithium storage. *ACS Appl. Mater. Interfaces* **2016**, *8*, 32853−32861.

[51] Yue, J.; Gu, X.; Jiang, X. L.; Chen, L.; Wang, N. N.; Yang, J.; Ma, X. J. Coaxial manganese dioxide@N-doped carbon nanotubes as superior anodes for lithium ion batteries. *Electrochim. Acta* **2015**, *182*, 676–681.

[52] Guo, D.; Zhang, H. M.; Yu, X. Z.; Zhang, M.; Zhang, P.; Li Q. H.; Wang, T. H. Facile synthesis and excellent electrochemical properties of $CoMoO_4$ nanoplate arrays as supercapacitors. *J. Mater. Chem. A* **2013**, *1*, 7247–7254.

[53] Jin, G. Z.; Xiao, X. X.; Li, S.; Zhao, K. M.; Wu, Y. Z.; Sun, D.; Wang, F. Strongly coupled graphene/Mn_3O_4 composite with enhanced electrochemical performance for supercapacitor electrode. *Electrochim. Acta* **2015**, *178*, 689–698.

[54] Zhao, Y.; Hu, L. F.; Zhao, S. Y.; Wu, L. M. Preparation of $MnCo_2O_4$@$Ni(OH)_2$ core-shell flowers for asymmetric supercapacitor materials with ultrahigh specific capacitance. *Adv. Funct. Mater*. **2016**, *26*, 4085–4093.

[55] Zhang, Y. B.; Wang, B.; Liu, F.; Cheng, J. P.; Zhang, X. W.; Zhang, L. Full synergistic contribution of electrodeposited three-dimensional $NiCo_2O_4$@MnO_2 nanosheet networks electrode for asymmetric supercapacitors. *Nano Energy* **2016**, *27*, 627–637.

[56] Wen, Y. X.; Peng, S. L.; Wang, Z. L.; Hao, J. X.; Qin, T. F.; Lu, S. Q.; Zhang, J. C.; He, D. Y.; Fan, X. Y.; Cao, G. Z. Facile synthesis of ultrathin $NiCo_2S_4$ nano-petals inspired by blooming buds for high-performance supercapacitors. *J. Mater. Chem. A* **2017**, *5*, 7144–7152.

[57] Zhang, X. D.; Cui, S. Z.; Wang, N. N.; Hou, H. W.; Chen, W. H.; Mi, L. W. Synergistic Effect Initiating $Ni_{1-x}Co_xMoO_4\cdot xH_2O$ as electrodes for high-energy-density asymmetric supercapacitors. *Electrochim. Acta* **2017**, *228*, 274–281.